polarity switching. They were taken at delay times of 0·1, 0·5, 0·9, 1·5 and 2 ms after the switching pulse (30 kV cm$^{-1}$). Each photograph is the result of 30 flashes. The gradual build-up of the strong (650) reflection is clearly evident. A series of experiments, performed with different field values, showed that the switching-time dependence upon the applied field was in good agreement with the values reported in the literature (Smith & Burns, 1969); it ranged from about 0·2 ms (at 40 kV cm$^{-1}$) to 5 ms (at 20 kV cm$^{-1}$).

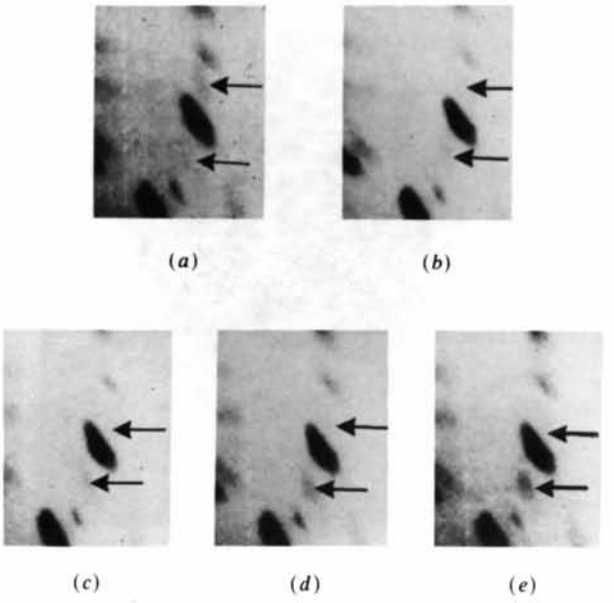


Fig. 2. Time development of domain switching in a GMO crystal. Portions of X-ray patterns recorded with increasing delay time after switching pulse: (*a*) 0·1, (*b*) 0·5, (*c*) 0·9, (*d*) 1·5 and (*e*) 2 ms.

To conclude, the experiments demonstrate that fast structural changes in single crystals can be reliably studied using flash X-ray diffraction techniques.

We thank Dr S. Starobinetz for helpful discussions and suggestions, Dr F. Frolow and Mr Y. Halfon for their contributions to the experimental work. We also would like to thank Mr G. Grimouille of the Centre National d'Etudes des Télécommunications, Paris, France, for providing us with some of the GMO crystals. This work was supported by grant No. 2451/81 from the United States–Israel Binational Science Foundation (BSF), Jerusalem, Israel.

### References

AIZU, K., KUMADA, H., YUMATO, H. & ASHIDA, S. (1969). *J. Phys. Soc. Jpn*, **27**, 511.
CUMMINS, S. E. (1970). *Ferroelectrics*, pp. 11–17.
FUJIMOTO, I. (1982). *Acta Cryst.* A**38**, 337–345.
GREEN, R. E. JR & RABINOVICH, D. (1984). *Flash Radiography Symposium*, pp. 157–170. Columbus, Ohio: The American Society for Nondestructive Testing.
IZUMI, T. (1975). *Jpn J. Appl. Phys.* **14**, 1581–1584.
IZUMI, T., INADA, K., NAKAJIMA, H. & KHORA, K. (1977). *Jpn J. Appl. Phys.* **16**, 1063–1064.
JEITSCHKO, W. (1972). *Acta Cryst.* B**28**, 60–76.
KUMADA, A. (1969). *Phys. Lett. A*, **30**, 186–187.
LOURIE, B. (1983). *Development of Flash X-ray Diffraction Techniques for Studies of Fast Effects in Single Crystals.* PhD. Thesis, Feinberg Graduate School, The Weizmann Institute of Science, Rehovot, Israel.
RABINOVICH, D., LOURIE, B. & HALFON, Y. (1987). *Rev. Sci. Instrum.* Submitted.
SMITH, A. W. & BURNS, G. (1969). *Phys. Lett. A*, **28**, 501–502.

*Acta Cryst.* (1987). B**43**, 504–512

## Superlattice Structure of Ferroelectric Barium Sodium Niobate (BNN)

BY PENG JU LIN AND L. A. BURSILL

*School of Physics, University of Melbourne, Parkville, Victoria* 3052, *Australia*

(*Received* 25 *March* 1985; *accepted* 9 *July* 1987)

### Abstract

Electron diffraction and high-resolution electron microscopy have been used to investigate the space group and structure of the commensurate superlattice phase of barium sodium niobate (BNN), $Ba_2NaNb_5BO_{15}$. At room temperature the space group appears to be *Im*2*a* with orthorhombic cell parameters $a = 35{\cdot}18$, $b = 35{\cdot}24$, $c = 7{\cdot}99$ Å. Use of dark-field beam-tilting techniques allow detection of weak symmetry elements and small atomic shifts associated with ordering of Ba and O atoms into pairs of sites which, according to X-ray studies, were assigned split occupancy. Structural models consistent with the above space group were derived and multislice techniques used to calculate the variation of subcell and supercell reflections, as well as the high-resolution images, with crystal thickness and orientation of the incident beam. Ordering of Ba ions, as well as *some* of the O ions, gave model-sensitive characteristics which could be tested by comparison with the experimental results.

0108-7681/87/060504-09$01.50 

## 1. Introduction

The physical properties of barium sodium niobate (BNN, $Ba_2NaNb_5O_{15}$) have been investigated thoroughly because of device applications related to its large non-linear polarizability (Lines & Glass, 1977). It has the tungsten-bronze-type framework structure and served as a prototype for over 150 individual end-member bronze compositions, with numerous possible solid solutions. Its structure has been extensively studied (Jamieson, Abrahams & Bernstein, 1969; Ikeda, 1974; Toledano, 1975; Schneck & Denoyer, 1981; Schneck, Toledano, Whatmore & Ainger, 1981; Manolikas, 1981*a*,*b*; Schneck, Toledano, Joffrin, Aubree, Joukoff & Gabelotard, 1982). An approximate symmetry of all the members of the structural family is represesented by the tetragonal space group $P4/mbm$ (No. 127) with parameters $a = 12{\cdot}4$, $c = 4$ Å. BNN exhibits a series of phase transitions. A standard ferroelectric transition ($4/mmm \rightarrow 4mm$) accompanied by a divergence of the dielectric susceptibility along **c** occurs at *ca* 853 K (Singh, Draggert & Geusic, 1970). At lower temperatures there are at least two structural transitions. The first, near 573 K, corresponds to the onset of an orthorhombic phase ($mm2$) which remains stable down to 113 K (Giess, Scott, Burns, O'Kane & Segmuller, 1969), when tetragonal symmetry may be recovered (Schneck, Primot, Ravez & Von der Muhl, 1977). The existence of two incommensurate superlattice phases was established by Schneck & Denoyer (1981). The upper transition near 561 K (Schneck *et al.*, 1982) corresponds to a phase having a doubled (8 Å) $c$ axis and an incommensurate modulation along a [110] tetragonal axis, giving orthorhombic symmetry ($a_o = 17{\cdot}59$, $b_o = 17{\cdot}63$, $c_o = 7{\cdot}99$ Å) for the average structure (Jamieson *et al.* 1969). The lower transition (523 K) leads to another phase with identical point symmetry ($mm2$) and the same direction of modulation, but with periodicity very close to four times the tetragonal [110]. This phase is stable at room temperature. Schneck *et al.* (1982) report that X-ray precession photographs of *single-domain* plates of BNN have systematic extinctions consistent with space group $Bbm2$. However, the X-ray data have not been published, nor has the superstructure been specified.

Manolikas (1981*a*) observed ferroelectric 180° domains and ferroelastic domains in the room-temperature phase of BNN, using electron diffraction contrast. The ferroeleastic domain walls were parallel to ⟨100⟩ of the tetragonal cell. Antiphase boundaries forming quadrupole joins were also reported, suggesting that at least four translation variants exist in the orthorhombic phase. Manolikas (1981*b*) also showed that $Sr_2KNb_5O_{15}$ (a structural analogue of BNN) contains irregular mixing of slab widths of 2× and 3× the orthorhombic subcell. Such a mixing may give rise to incommensurate superlattice reflections, depending on the volume fractions of different slab widths (Fujiwara, 1957; Grzinic, 1985).

Electron diffraction data are hereby reported which have allowed the reciprocal-lattice geometry of BNN to be more fully explored. The relatively large atomic scattering factors of electrons ($f_e = 10^4 f_{\text{X-ray}}$) have revealed orthorhombic supercell parameters $a = 35{\cdot}18$, $b = 35{\cdot}24$, $c = 7{\cdot}99$ Å. The space group $Im2a$ (No. 46) is consistent with (i) the observed electron diffraction patterns and high-resolution images; (ii) the tetragonal tungsten-bronze (TTB) framework structure; and (iii) the observed ferroelectricity. High-resolution images, obtained by deliberate use of beam-tilting techniques and careful choice of observed aperture and crystal thickness, were used to reveal the periodic antiphase nature of the superstructure.

The model sensitiveness of both high-resolution images and electron diffraction data were tested by computer simulations.

## 2. Experimental

Single-crystal boules of $Ba_2NaNb_5O_{15}$ were sliced and mechanically thinned parallel to (001), (100) and (110). Thin sections (~80 μm) were chemically thinned and polished for electron microscopy by immersion in molten $KHSO_4$, using a platinum crucible at 723–773 K. Washed and dried specimens were then sandwiched between two 75-mesh copper grids. Electron diffraction patterns were recorded for $93 < T < 423$ K using a JEOL-100CX instrument fitted with a Gatan double-tilting (±30°, ±10°) heating–cooling goniometer. The room-temperature phase was studied in a high-tilt goniometer (±60°, ±45°). Beam divergences $\leq 10^{-4}$ rad were used to obtain sharp diffraction patterns. Weak superlattice reflections were recorded using exposure times of up to 120 s, using Kodak AA Industrex X-ray film. High-resolution bright- and dark-field images were obtained using top-entry goniometers, either at 100 kV ($C_s = 0{\cdot}7$ mm) or at 200 kV ($C_s = 0{\cdot}95$ mm) using JEOL instruments, fitted with 5, 10, 20 and 40 μm objective apertures. This part of the work was restricted to room temperatures.

## 3. Results

### (*a*) *Electron diffraction*

The observed reflections are represented in Fig. 1. Indices refer to an orthorhombic unit cell with $a = 35{\cdot}18$, $b = 35{\cdot}24$, $c = 7{\cdot}99$ Å, with $a = 2a_o$, $b = 2b_o$, $c = c_o$, referred to the cell of Jamieson *et al.* (1969). Starting with [110], it was possible to record both [100] and [010] reciprocal-lattice sections from the same area of crystal by tilting through ±45°. Many intermediate zone-axis patterns could be recorded.

Fig. 1 was established finally by systematic tilting experiments, starting with [100] and [010]. These gave quite distinct diffraction patterns (Figs. 2*a*,*b*). Note that for [010] the superlattice spots 101, 301 have very much greater intensity, relative to the subcell spots, than do the superlattice spots 011 and 031 for [100]. In fact, diffraction patterns identical to Figs. 2(*a*), (*b*) were also recorded for adjacent domains, separated by a ferroelastic domain wall. This result is slightly different from the behaviour reported by Schneck & Denoyer (1981). Our result is that, whilst the second modulation direction is weak, it is not zero. Despite careful tilting experiments, it was not possible to obtain zero intensity for $0kl$, $k+l=2n$ ($k$, $l$ odd) reflections. However, considerable variations of intensity occurred with slight changes in crystal and incident-beam tilt, suggesting these reflections are due either to upper-layer dynamical interactions or to a very weak symmetry element giving rise to weak reflections which in turn are also strongly affected by upper-layer dynamical interactions. Use of convergent-beam electron diffraction techniques was not appropriate for the study of these weak superlattice reflections. It was decided to treat these observations as indicating a slight departure from the precise *b*-glide condition, implied by the X-ray result of Schneck & Denoyer (1981).

The observations for [001] showed allowed reflections $hk0$; $h, k=2n$. As indicated in Fig. 1, the sequence of zone axes [100], [101], [102],..., obtained by a tilt series about [010], as well as the sequence [010], [011], [012],..., obtained by a tilt series about [100], clearly demand $a=2a_o$, $b=2b_o$. Note that for the former series the superlattice spots are alternatively weak-strong-weak-..., whereas for the latter they are strong-weak-strong-.... For example, Figs. 2(*c*), (*d*) show the relatively strong superlattice spots for [101] and [012]. For [102] and [011] projections, the superlattice spots were relatively very weak (*cf.* [100], Fig. 2*b*).

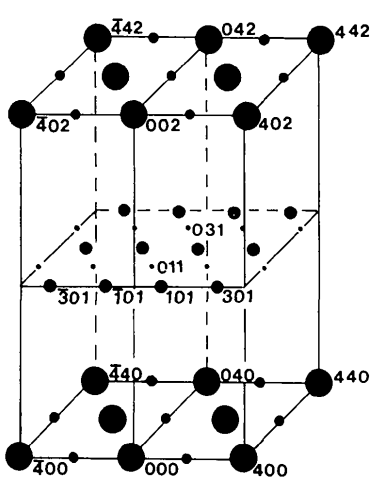


Fig. 1. Reciprocal-lattice model for BNN (at room temperature), constructed using electron diffraction patterns for [001], [010], [100], [101] and [102] zone-axis projections. Indices refer to an orthorhombic superlattice cell having parameters $a=35{\cdot}18$, $b=35{\cdot}25$ and $c=7{\cdot}99$ Å.

Note that it is essential to use pure single-domain areas of crystal to establish Fig. 1, as even a small fraction of parasitic second-orientation domains will give readily visible superlattice spots for all zones in both sequences. The temperature variation of the superlattice intensities is also important. Specimens which have been heated to $\geq 573$ K and then cooled quickly (in a few minutes) to room temperature may show poorly developed superlattice reflections (*i.e.* which are weak and less sharp for *all* zone axes in the tilt sequences referred to above). On the other hand, cooling to 113 K may lead to a sharpening of spots and more pronounced weak-strong-weak-... sequences for tilt series starting at [010] and strong-weak-strong-... sequences for tilt series starting at [100]. Finally, at 105 K, there is a sharp phase transition, with the appearance of additional superlattice spots for [101] zone-axis patterns. A further report of the temperature variation of electron diffraction patterns for BNN, in the range $93<T<423$ K is in preparation (Bursill & Peng).

### (*b*) *Space-group assignment*

Earlier attempts to use space groups *Cmm*2 (Jamieson *et al.*, 1969), $Ccm2_1$ (Toledano, 1975), or *Bbm*2 (Schneck, Toledano, Whatmore & Ainger, 1981) assumed either the $17{\cdot}1\times17{\cdot}7\times8$ Å subcell or a $35{\cdot}2\times17{\cdot}6\times8$ Å subcell. Use of the $35{\cdot}2\times35{\cdot}2\times8$ Å cell deduced above (Fig. 1), with the observed extinction conditions

$$\begin{array}{llll} hkl: & h+k+l=2n & h00: & h=2n \\ 0kl: & k+l=2n & 0k0: & k=2n \\ h0l: & h+k=2n & 00l: & l=2n \\ hk0: & h,k=2n & & \end{array}$$

leads to the possible space groups *Im*2*a* (No. 46) or *Imma* (No. 74) (see Table 3.2, *International Tables for Crystallography*, 1983). *Imma* can be eliminated since its centrosymmetric space group is incompatible with the known ferroelectricity of BNN at room temperature. It was decided to proceed with structural analysis using space group *Im*2*a*.

### (*c*) *Dark-field diffraction contrast studies*

As shown by Manolikas (1981*a*), there should be four orientation variants of orthorhombic BNN, corresponding to the two possible orientations of the polar orthorhombic *c* axis with respect to the tetragonal *c* axis and two possible orientations of the orthorhombic *a* axis. The former give rise to ferroelectric 180° domains, whereas the latter give rise to

ferroelastic domains. Dark-field observations readily identified ferroelectric domains as shown by strong changes in background contrast and wedge fringes due to inclined 180° domain walls (Bursill & Peng, 1986*a*).

Ferroelastic domains were found only rarely in our boule, indicating the extent of any one ferroelectric orientation to be ~1 μm, at least. Dark-field observations failed to reveal a fine-scale domain texture. These observations are consistent with the electron diffraction results that tilting from [010] to [100] showed markedly different intensities for the superlattice, relative to the subcell, reflections. Similar imaging studies of barium strontium niobate (SBN) showed readily a fine-scale domain texture with domain diameters ~100–200 Å (Bursill & Peng, 1986*b*). Intergrowth defects or discommensurations were not observed in BNN at room temperature. This is compatible with our observation that the superlattice spots in [010] projections were commensurate within experimental error (≤1%). This result contrasted markedly with the behaviour of SBN, which is incommensurate at room temperature and showed a high density of intergrowth defects, on the scale of about one every $3 \times d_{010}$ (Bursill & Peng, 1986*b*).

### (*d*) *High-resolution images*

Zone-axis bright-field images for [001] and [100] proved insensitive to the superstructure, as expected, owing to the dominance of the subcell reflections [see § 4(*a*) below]. However, it was possible to emphasize the superstructure by deliberate use of beam-tilt controls to obtain high-resolution bright- and dark-field

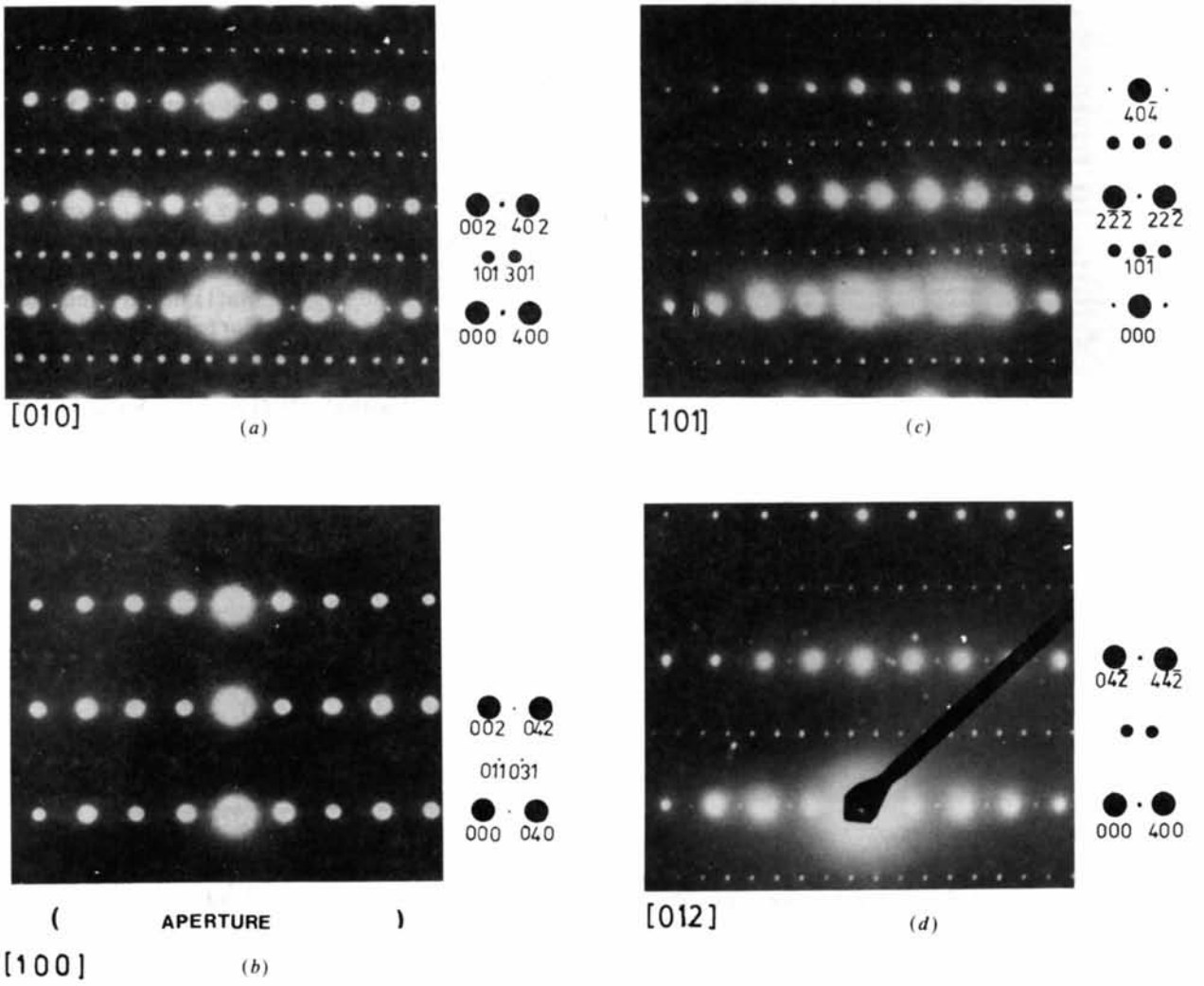


Fig. 2. (*a*) [101], (*b*) [010], (*c*) [100] and (*d*) [001] zone-axis electron diffraction patterns for BNN at room temperature. The diameter of the objective aperture used for HREM is indicated.

images for asymmetrically excited [010] zone axes. Fig. 3(*a*) shows a high-resolution bright-field image (aperture size indicated in Fig. 2*b*) for a [010] projection after tilting the incident beam by approximately 3 mrad towards [001]. Note the strong thickness dependence of the image contrast. For a range of thickness spanning the second extinction contour, the images show clearly a doubling of the *c* axis (8 Å) with periodicity 35·2 Å along the orthogonal axial direction. Enlargement of this region (Fig. 3*b*) reveals a periodic antiphase structure, with alternate 17·6 Å slabs having relative displacement [001]. Other examples of high-resolution beam-tilted images were obtained: many dark-field conditions were discovered, for a wide range of beam-tilt conditions, for which the superstructure repeats of $2\times d_{100}$ and $2\times d_{001}$ could be visualized. However, no doubling of the *b* or *c* axes could be detected for [100] images, even with beam tilt (Fig. 3*c*): this is consistent with the very weak superstructure reflections observed for this projection (see Fig. 2*b*). One-dimensional images, obtained using only three collinear supercell spots showed a regular 17·6 Å modulation of the basic structure, extending over >0·5–1·0 μm.

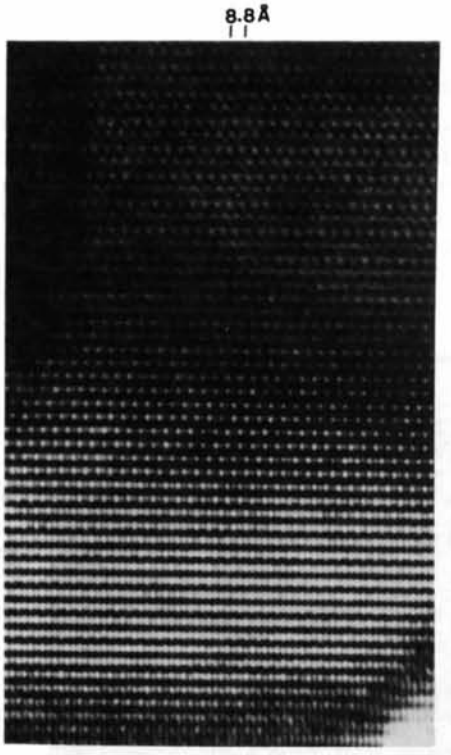


(*a*)

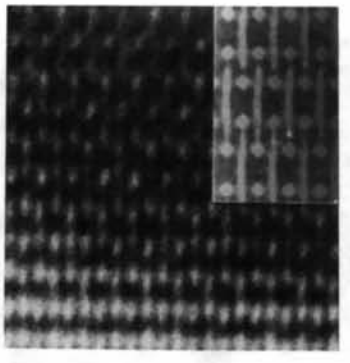

(*b*)

Fig. 3. (*a*) High-resolution bright-field image of BNN, with beam tilt towards [001] for [010] projection. Note appearance of *c*-axis doubling and repeat of 35·2 Å along orthogonal [100] axis for the thicker crystal regions, within the dark extinction contour. (*b*) Enlargement of (*a*) showing fine detail of superstructure. Note periodic antiphase operation every 17·6 Å with white spots and streaking along [100]; also *c*-axis doubling. Inset in (*b*) shows image match for structural solution proposed in § 4 (*cf.* Fig. 5).

## 4. Structural considerations

### (*a*) *X-ray structure for BNN*

This is shown in Fig. 4. Labels refer to sites having different atomic nature and point symmetries, according to atomic coordinates given by Jamieson *et al.* (1969). That refinement used the space group *Cmm*2 with unit-cell parameters $a_o = 17{\cdot}59$, $b_o = 17{\cdot}63$, $c_o = 3{\cdot}989$ Å. That the true cell is larger than this, actually $2a_o, 2b_o, 2c_o$, is indicated by the apparent disorder for atoms with $z = 0{\cdot}5$. Thus, Ba(1) lies to either side of the mirror plane perpendicular to the orthorhombic *a* axis (Fig. 4), with two alternative positions separated by a distance of 0·283 Å. Ba(2) lies on the mirror plane associated with the 4(*d*) position, having qualitatively different symmetry from Ba(1), which is in a general 8(*f*) position. The symmetry of the O(10) and O(9) atoms differs only quantitatively, with the O(10)

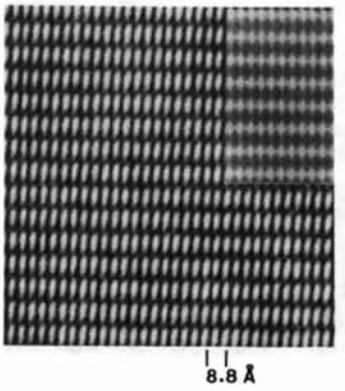


(*c*)

Fig. 3 (*cont.*) (*c*) High-resolution bright-field image of BNN for [100] projection, no *c*-axis or *b*-axis doubling could be detected, regardless of crystal or beam tilt. The inset shows the image match for the structural model proposed in § 4.

sites separated by 0·380 Å and the O(9) sites by 0·556 Å. The remaining O atoms (7) and (8) are 'split', by 0·580 Å for O(7*a*,*b*) and 0·499 Å for O(8*a*,*b*). It was suggested that the disorder may be associated with the [$NbO_6$] octahedra, so that along **c** Nb–O–Nb angles are reduced from 180 to 165°. An ordered arrangement of tilted (Jamieson *et al.*, 1969; Fig. 3) or cooperatively sheared (Schneck *et al.*, 1982; Fig. 14) octahedra leads to a doubling of the *c* axis. The O atoms around Ba form a distorted tricapped trigonal prism. The Na atom has distorted cubo-octahedral coordination.

All of the metal atoms in BNN are displaced along **c** from the nearest mean plane of O atoms, in the same sense, which provides the origin of ferroelectricity and determines the macroscopic polarity. There are two independent mean planes of O atoms, at $z = 0{\cdot}0423$ and $z = 0{\cdot}4543$ (*i.e.* $\frac{1}{2} - 0{\cdot}0457$). The ferroelectric properties seem to be determined primarily by the $Nb^{5+}$ displacements (0·178–0·205 Å) with respect to these oxygen mean planes (Jamieson *et al.*, 1969; Fig. 1).

### (*b*) *Derivation of structural model for superstructure*

In order to accommodate the [$NbO_6$] octahedral framework of BNN, the mirror plane (*m*) and diagonal glides (*n*) of space group *Im*2*a* (Fig. 5) must bisect the split Ba(1) sites (Fig. 5). The asymmetric unit $0 < x < \frac{1}{4}$; $0 \le y \le \frac{1}{2}$; $0 \le z \le 1$ contains two Na atoms, each at the centre of a unit of eight [$NbO_6$] octahedra. The coordination of Na then resembles that of Ca in perovskite. However, the presence of split sites O(7*a*,*b*) and O(8*a*,*b*) implies the Na coordination is not strictly cubooctahedral.

The ordering of O(7*a*,*b*) sites, as shown in Fig. 5, was derived following a systematic consideration of possible sheared-octahedral combinations, which must be consistent with the symmetry operations of *Im*2*a*. Figs. 6(*a*), (*b*) show the two distinct [010]-bounded sections ($0 \le y \le \frac{1}{4}$ and $\frac{1}{4} \le y \le \frac{1}{2}$ respectively) required to describe the framework of the superstructure (*cf.* Fig. 5). The periodic antiphase operation, which occurs every 17·6 Å, as indicated by the white-spot arrangement of Fig. 3(*b*), is represented by large open circles in Fig. 6(*c*), which shows the superposition of Figs. 6(*a*), (*b*). Note that the periodic antiphase is consistent with a set of octahedral shears which create a sequence of relatively open and relatively closed tunnels alternating along **c**. The particular arrangement selected for Fig. 6(*c*) produces maximum alternation of open and closed spaces along **c**. On referring back to the [001] projection (Fig. 5), we see that this corresponds to concerted clockwise (*C*) and anticlockwise (*A*) rotatory displacements of the O(7*a*,*b*), O(8*a*,*b*) sites associated with each column of four [$NbO_6$] octahedra, where *C* and *A* rotations alternate along **c** (Fig. 5). Thus,

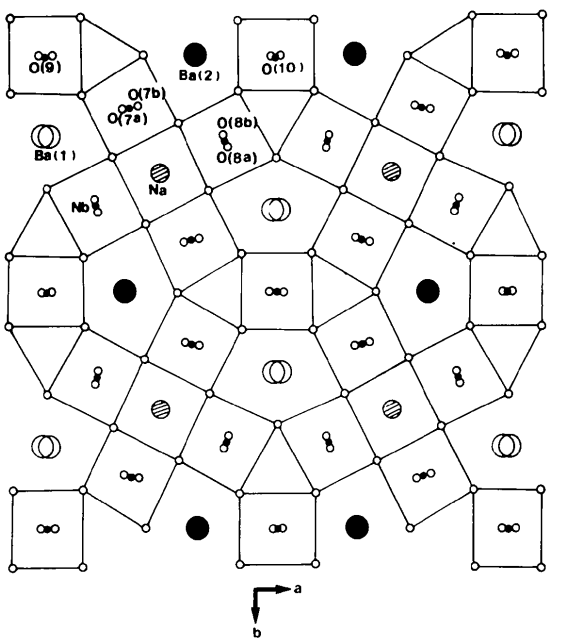


Fig. 4. X-ray structure of BNN (after Jamieson *et al.*, 1969). Note especially the location of split sites [Ba(1), O(7), O(8) and O(9), O(10)].

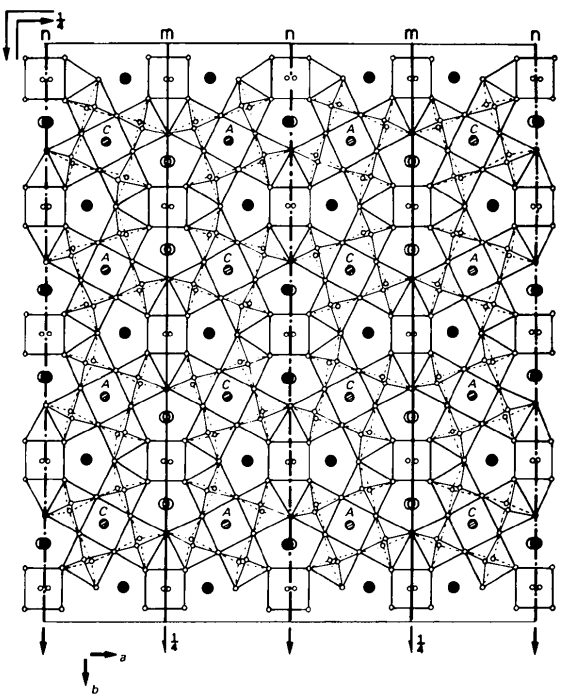


Fig. 5. Location of symmetry elements of space group *Ibm*2 on [001] projection of BNN allows the mirror plane (*m*) to be located through Ba(2) sites and 2 and $2_1$ axes through O(9), O(10) sites. Ordering of O(7*a*,*b*), O(8*a*,*b*) sites was deduced from Fig. 3(*b*). Note the concerted rotation of oxygen groups of four octahedral colums, alternately clockwise (*C*) and anticlockwise (*A*) about the *c* axis, with sequence *CAAC* along [100] and *CACA* along [010].

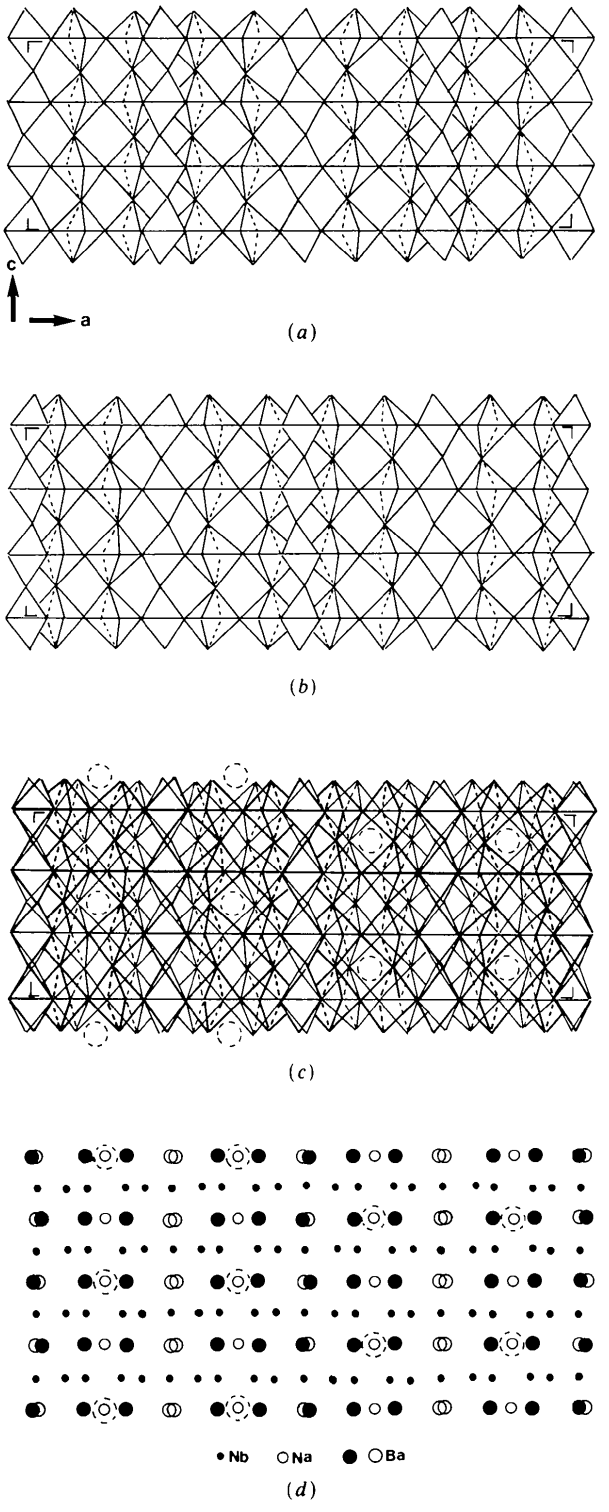


Fig. 6. Two [010] bounded sections, (*a*) $0 \le y \le \frac{1}{4}$ and (*b*) $\frac{1}{4} \le y \le \frac{1}{2}$, required to describe the superstructure of ordered O-atom sites. (*c*) Superposition of (*a*) and (*b*) showing development of a periodic antiphase arrangement of relatively open spaces (larger dotted circles) due to cooperative O-atom displacements. (*d*) Location of Ba, Nb and Na ions in superstructure relative to oxygen octahedra. The periodic antiphase operation again appears (note equivalence of structure about dotted circles).

we are led to a remarkably simple structural element, consisting of alternating *C* and *A* rotations of groups of four O atoms at levels $z = 0, \frac{1}{2}$, along **c**. Such concerted rotations provide a very symmetrically coordinated environment for the Na atom (or for Sr in SBN). Other combinations of octahedral shearing, consistent with *Im*2*a*, lead to a mixture of asymmetrically placed Na–O bond lengths and angles.

The *m* and *n* operations of *Im*2*a* generate automatically the sequence *CAACCAC* along [100] (Fig. 5) and the 2 and *a*-glide operations also generate this same sequence along [010] (Fig. 5), regardless of choice *CA*, *CC* or *AA* for the asymmetric unit.

It remains to consider assignment of ordering for the remaining split sites Ba(1), O(9) and O(10). Inspection of the location of Ba(1) (split) sites, with respect to the mirror (*m*) and glide (*n*) planes leads to the conclusion that only those split sites bisected by the glide plane *n* need be ordered (Fig. 5). Here again the displacements along [100] are determined by the space-group operations so that the displacements oppose on alternate *n*-glide planes. The ordering of displacements along [010] was decided by consideration of the high-resolution image (Fig. 3*b*). Alternation would lead to the loss of the antiphase operation in the image for the [010] projection, as verified by computer simulations (see § 5 below). Thus all the Ba atoms in any one (100) plane are displaced in the same, rather than alternating left/right, senses. This corresponds to condensation of a simple one-dimensional longitudinal modulation wave along [100].

The Ba sites bisected by the mirror operations (*m*) (Fig. 5) must be supposed to remain split (disordered, half-occupancy) or else shift directly onto the mirror plane. It is clearly not possible to settle this point using the high-resolution image alone, since the projected potential is virtually identical in the two cases, at least for 3 Å resolution. However, the observation of a further phase transition of BNN at 105 K, with readily visible effects on the electron diffraction patterns, is quite consistent with a second stage of Ba site ordering at the lower temperature. It was therefore decided to allow half of the Ba split sites (*i.e.* those bisected by the *m* operation) to remain disordered in our model for the room-temperature phase. The [010] projection of all the cation sites of our model (Ba, Na and Nb) is shown in Fig. 6(*d*).

Since the high-resolution image proved insensitive to ordering of O(9) and O(10) sites, we have preferred to leave these with split occupancy in our structural model at this stage, since there are several possible choices available within the asymmetric unit.

## 5. Image calculations

HREM images were simulated using standard multislice techniques (Goodman & Moodie, 1974). Eight

slices, each of thickness 4 Å, were required for the [010] and [100] projections. The image matches obtained are inset in Fig. 3(*b*) for [010] and Fig. 3(*c*) for [100]. The images, with beam- and crystal-tilt effects included, proved to be remarkably sensitive to the Ba ordering and modulation direction, as shown by a comparison of the images expected for the X-ray structure with that obtained for the *Im*2*a* model. This behaviour is made clear by comparing intensity *versus* thickness plots for the transmitted and some low-order subcell and superlattice reflections. Thus, the transmitted *and* 002 beams oscillate with periodicity ~200 Å for both X-ray and ordered superstructure models. The superlattice reflections 101, 301 and 200, 202 and their symmetry equivalents show a general tendency to reach maxima for $400 \leq H \leq 700$ Å (Figs. 7*a*,*b*). Thus, the influence of these reflections is strongest for this range of thickness, where the transmitted beam is relatively low. Note that the Ba ordering provided by far the major contribution to the superstructure reflection intensity. Ordering of O(7), O(8) makes significant contributions (~20% of that due to Ba ordering) along [010]. Intensity *versus* thickness plots for the [100] projection showed that the subcell reflections are almost indistinguishable from those for [010]. Superstructure reflections 011 and 031 have intensity comparable to 101 and 301 for O(7), O(8) ordering (Fig. 7*a*) but are only ~20% of 101 and 301 for both Ba and O(7), O(8) ordering (Fig. 7*b*), consistent with Figs. 2(*a*), (*b*).

The effects of crystal tilts on the transmitted and scattered beam intensities are shown in Fig. 8. Tilts so that the centre of the Laue circle reaches 000 (*A*), 001 (*B*) and 001 (*C*) are shown for 002 beams

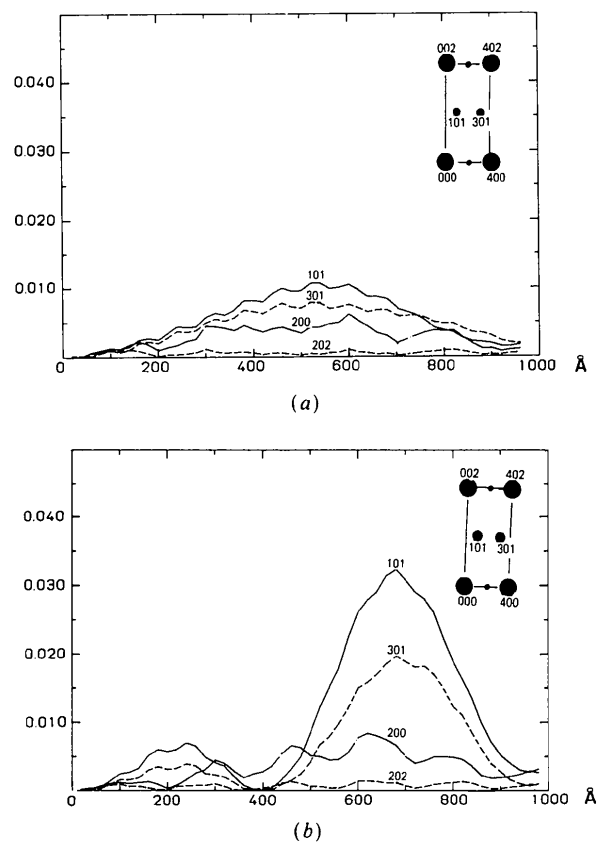


Fig. 7. Intensity *vs* thickness plots for supercell reflections (101, 301, 200, 202) of BNN. (*a*) Refers to ordering of O(7), O(8) only; (*b*) refers to ordering of O(7), O(8) plus ordering of Ba(1).

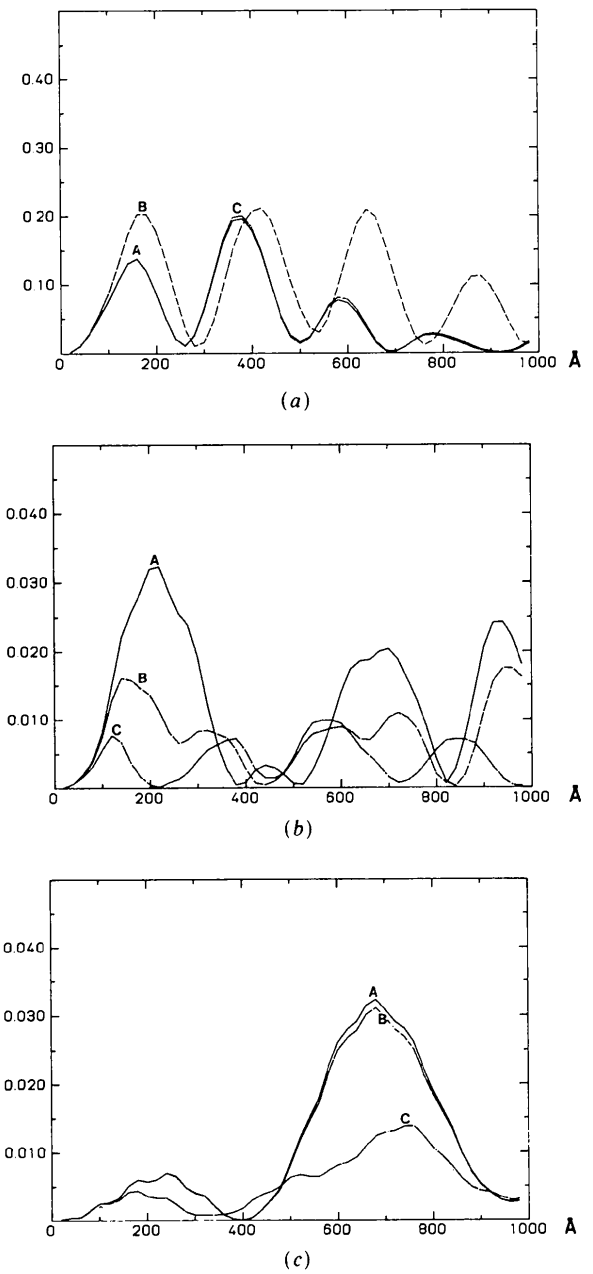


Fig. 8. Intensity *vs* thickness plots showing the effect of crystal tilts. The Laue-circle centre was located at 000 (*A*), 001 (*B*), or 002 (*C*). (*a*) Refers to 002 beams; (*b*) refers to 400 beams and (*c*) refers to 101 beams.

(Fig. 8*a*), for 400 beams (Fig. 8*b*) and for 101 and 301 beams (Fig. 8*c*). Differences become very apparent for crystal thicknesses 100–400 and 600–1000 Å for the 400 subcell reflection (Fig. 8*b*). Significant changes occur for all thickness for the subcell reflection 002 (Fig. 8*a*). The important supercell reflections 101 and 301 change most for thickness 500–900 Å, although there are also changes for 100–350 Å (Fig. 8*c*).

Image calculations, including both *beam* and crystal tilts, were quite sensitive to beam-tilt conditions and, in order to obtain a reasonable image match, beam tilt of the Laue circle to 001 (3 mrad) was required (inset Fig. 3*b*) for crystal thicknesses 200–240 Å. Deliberate introduction of beam tilt tends to give enhanced contrast for the superstructure, especially for crystal thicknesses ≥400 Å. However, a thinner region (~220 Å) was selected for image matching since there may be some concern that inelastic scattering effects may complicate the interpretation of the images for thicker crystals.

Whilst the image matching is expected to be quite sensitive to the ordering of Ba(1) sites, it is not expected to test fully the model for ordering of O(7), O(8) or O(10) sites (*cf.* Figs. 7*a,b*). Note, however, that the weak 020 and 022 reflections, predicted and observed for [100] (Fig. 2*c*), are due only to O(7), O(8) ordering, since the displacements of Ba(1) and O(9), O(10) lie parallel to this projection. This observation confirms that there is significant supercell ordering of O(7), O(8) sites.

## 6. Concluding remarks

Use of electron diffraction to detect weak superlattice reflections, in combination with high-resolution beam-tilt imaging, has allowed a space group to be assigned for the room-temperature form of BNN. A structural model was derived which is consistent with (i) the X-ray structure due to Jamieson *et al.*; (ii) the space group *Im*2*a*, with superlattice cell parameters $a = 35{\cdot}18$, $b = 35{\cdot}24$, $c = 7{\cdot}99$ Å; and (iii) the computer-simulated images. The ordering proposed for Ba(1) and O(7*a,b*), O(8*a,b*) sites was tested by image matching for the [010] projection and by the relative intensities predicted for superlattice reflections for the [010] and [100] projections. Ordering of O(9), O(10) sites remains to be determined, since the HREM images or electron diffraction intensities are not model sensitive. Further study of the Ba- and O-site orderings may be pursued more efficiently, perhaps, by X-ray or neutron diffraction studies. Since the space group or the commensurate superlattice is now defined more completely, it should be worthwhile to search again for appropriate data (weak reflections) using these techniques.

This work was supported by the Australia Research Grants Scheme and the University of Melbourne.

### References


BURSILL, L. A. & PENG, J. L. (1986*a*). *Ferroelectrics*, **70**, 191–203.

BURSILL, L. A. & PENG, J. L. (1986*b*). *Philos. Mag.* **54**, 157–170.

FUJIWARA, K. (1957). *J. Phys. Soc. Jpn*, **12**, 7–13.

GIESS, E. A., SCOTT, B. A., BURNS, G., O'KANE, D. F. & SEGMULLER, A. (1969). *J. Am. Ceram. Soc.* **52**, 276–280.

GOODMAN, P. & MOODIE, A. F. (1974). *Acta Cryst.* A**30**, 280–288.

GRZINIC, G. (1985). *Philos. Mag. A*, **52**, 161–187.

IKEDA, T. (1974). *Jpn J. Appl. Phys.* **13**, 1065–1071.

*International Tables for Crystallography* (1983). Vol. A. Dordrecht: D. Reidel.

JAMIESON, P. B., ABRAHAMS, S. C. & BERNSTEIN, J. L. (1969). *J. Chem. Phys.* **49**, 4352–4363.

LINES, M. E. & GLASS, A. M. (1977). *Principles and Applications of Ferroelectrics and Related Materials.* Oxford: Clarendon Press.

MANOLIKAS, C. (1981*a*). *Ferroelectrics*, **34**, 235–237.

MANOLIKAS, C. (1981*b*). *Phys. Status Solidi A*, **68**, 653–660.

SCHNECK, J. & DENOYER, F. (1981). *Phys. Rev. B*, **23**, 383–388.

SCHNECK, J., PRIMOT, J., RAVEZ, J. & VON DER MUHL, R. (1977). *Solid State Commun.* **21**, 57–59.

SCHNECK, J., TOLEDANO, J. C., JOFFRIN, C., AUBREE, J., JOUKOFF, B. & GABELOTARD, A. (1982). *Phys. Rev. B*, **25**, 1766–1785.

SCHNECK, J., TOLEDANO, J. C., WHATMORE, R. & AINGER, P. W. (1981). *Ferroelectrics*, **36**, 327–329.

SINGH, S., DRAGGERT, D. A. & GEUSIC, J. E. (1970). *Phys. Rev. B*, **2**, 2709–2716.

TOLEDANO, J. A. (1975). *Phys. Rev. B*, **30**, 943–950.